Earth Sciences
2022; 11(3): 121-129
http://www.sciencepublishinggroup.com/j/earth
doi: 10.11648/j.earth.20221103.18
ISSN: 2328-5974 (Print); ISSN: 2328-5982 (Online)

Detection of Uranium Anomalies and Alteration Zones Using Airborne Gamma-Ray Spectrometry at Gabal Attala and Its Surrounding Area, Eastern Desert, Egypt

Ahmed Tarshan

Airborne Geophysics Department, Exploration Division, Nuclear Materials Authority, Cairo, Egypt

Email address:
ahmed_ramadan_geo@hotmail.com

To cite this article:
Ahmed Tarshan. Detection of Uranium Anomalies and Alteration Zones Using Airborne Gamma-Ray Spectrometry at Gabal Attala and Its Surrounding Area, Eastern Desert, Egypt. *Earth Sciences*. Vol. 11, No. 3, 2022, pp. 121-129. doi: 10.11648/j.earth.20221103.18

Received: May 26, 2022; **Accepted**: June 16, 2022; **Published**: June 27, 2022

Abstract: Gamma-ray spectrometry method is widely used in various fields. The study area is located in the Central Eastern Desert of Egypt and covers about 1200 square kilometers. The rock units in the study area can be organized in ages from the Precambrian (mainly granite) to Quaternary. Airborne gamma-ray spectrometry data were collected by Aero-Service, 1984. The main objectives of this study are to detect hydrothermal alteration zones and the uranium anomalies in the study area. The processing of the data was conducted to generate radioactive element concentration maps (K, eU and eTh). Hydrothermal alteration zones such as potassic and phyllic altered areas were detected using the Potassium Ternary Composite Image map and the eTh/K map. The F-parameter technique and K ideal method were used to determine the locations of the potassium-enrichment. These locations are characteristically associated with the orogenic gold mineralization in the study area. Fourteen radioactivity zones were classified based on the Interpreted Radio-Spectrometric Zonation (IRSZ) Map. These zones were divided into high, medium and low radioactive response where zones of high radioactive response were revealed as zones 1, 6, 9 and 13. Uranium anomalies have been identified as these anomalies are abundant in eU values and also associated with higher values of eU/eTh and eU/K, where the maximum value of eU is associated with the Younger Granite with a value of 18.831 ppm. These uranium anomalies are associated with Taref Formation, Post-Hammamat felsite, Quaternary deposits and Younger Granite. The locations of uranium anomalies are considered important exploration targets, as these locations are promising and have priority for ground geophysical and geological follow-up.

Keywords: Airborne Gamma-Ray Spectrometry, Uranium, Radioactivity, Eastern Desert of Egypt

1. Introduction

Gamma-ray spectrometry method is widely used in various fields. It can be used in uranium exploration, in addition to using this method in geological mapping [1-5], mineral exploration [5-7], soil mapping [5, 8, 9], and environmental radiation monitoring [5, 10-12].

Information about soil, regolith, and geomorphological studies can be obtained through the airborne gamma ray spectrometry method and used in land management and mineral exploration decisions [9].

Due to the different concentrations of radioelements for each rock type, contacts between the different lithologies can be detected using concentrations calculated from measured gamma-ray spectrometry data [13, 14].

Airborne gamma-ray spectrometry measures the richness of potassium, thorium and uranium (K, eTh, eU) through determining gamma rays emitted by the decay of the naturally occurring radioactive elements of these elements in weathered rocks and materials. K richness is measured directly as gamma rays are emitted when 40K decays into argon.

It is difficult to measure the richness of uranium and thorium directly. It can be measured during the decay of the parent elements through measuring the daughter nuclides that are produced, and inferring the richness of the parent elements. The distinguished emission peaks associated with 208Tl and 214Bi are used to calculate the concentration of thorium and uranium (Figure 1).

Airborne gamma ray spectrometry data were collected and interpreted over the Gabal Atalla and its surrounding area,

Central Eastern Desert of Egypt. An assessment is performed of the distribution of radioactive minerals in different rock units, in addition to localization of the promising sites for uranium occurrences.

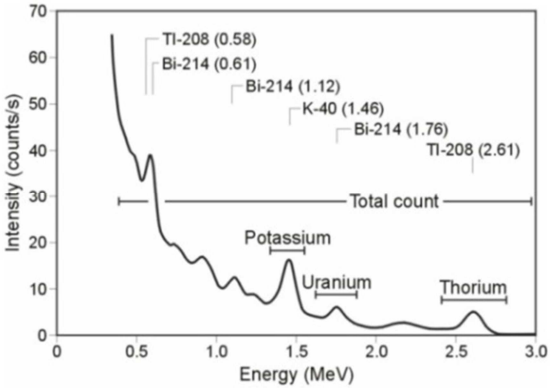

Figure 1. *Gamma-ray spectrum showing the position of the K, Th, U and total count windows [16].*

2. Data Collection

An Aero-Service aircraft was used in 1984 [17] for data acquisition, equipped with a 256-channel (12 kV/channel) gamma-ray spectrometer system used for measurement of the study area. The study area is located between longitude 33° 12′ 43.61″ to 33° 37′ 50.77″ E and latitude 25° 53′ 31.85″ to 26° 23′ 11.88″ N.

The detector system consists of a primary detector (downward-looking) to measure terrestrial gamma radiation and a secondary detector to measure the atmospheric radon. The primary detector includes three packages; each one consists of four high-resolution sodium iodide crystals with individual dimensions of 4x4x16 inches. A variety of analog outputs can be selected from the Data Acquisition System (CODAS) developed by Aero-Service, 1984 [17] by the system operator. The outputs for this survey were, total count (0.6-3.0 MeV), potassium (40K) (1.37-1.57 MeV), uranium (214Bi) (1.67-1.87 MeV), thorium (208Tl) (2.41-2.82 MeV), and a radar altimeter (100 feet/inch≈12 m/cm) [18].

3. Geologic Setting

The basement complex in the Egyptian Eastern Desert is part of the Arabian-Nubian Shield that stretches from Ethiopia and Uganda in the south to Egypt in the north. The occurrence of ophiolites and their association with calc-alkaline rocks of island-arc affinity proved that the continental crust formed by microplate accretion relevant to tectonic subduction and collision processes during the pan-African orogenic event [19, 20].

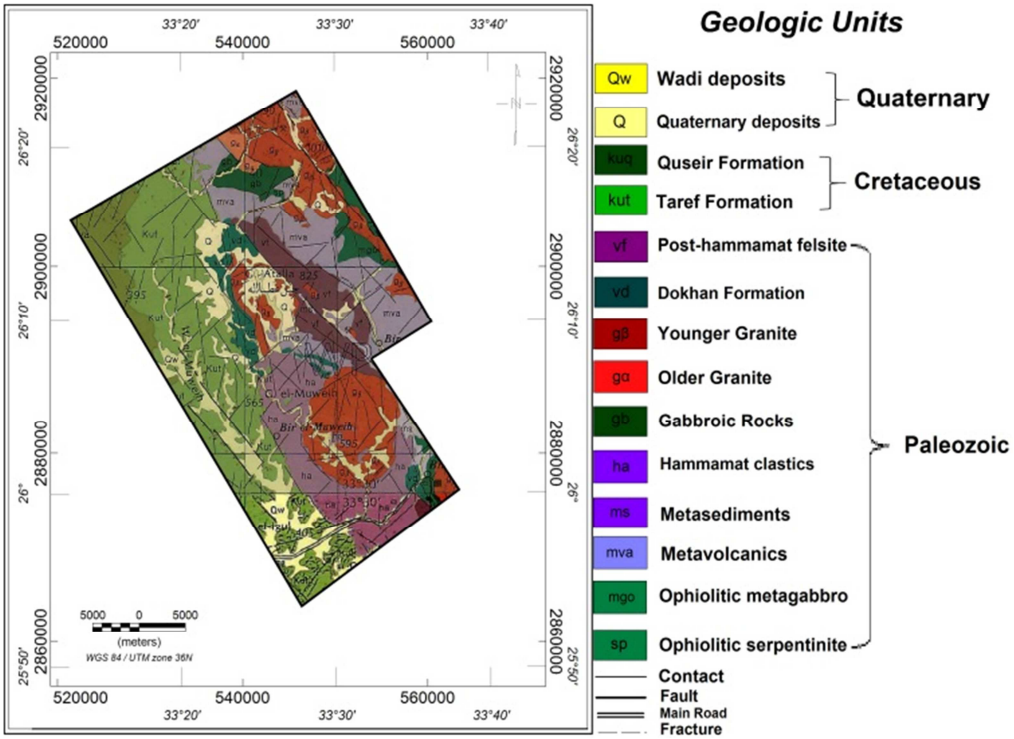

Figure 2. *Geologic Map of Gabal Attala and its surrounding area, Central Eastern Desert, Egypt [28].*

A huge mass of alkaline granites and volcanic rocks were emplaced during the post-orogenic stage. The abundance of east-to-northeast-trending dikes, clastic sedimentary basins, and volcanic fields with similarly oriented axes indicate that the crust was actively extending during at least the period 600–575 Ma using Rb/Sr and U/Pb ages [20, 21]. In addition to that K/Ar ages in the period between 530–480 Ma were detected from dike swarms located north of Qena-Safaga road in the Central Eastern Desert [20, 22].

During the early Paleozoic, post-Pan African magmatic

activity occurred in interrupted form, with intrusions and extrusions from the Ordovician-Devonian periods. In the late Carboniferous and Permian-Triassic era, three major volcanic rings intruded as ring complexes, sills, dikes, and sheets. [20, 23, 24].

The geological background of the Eastern Desert of Egypt is divided by two fault zones that divide it into three distinct basement domains; North Eastern Desert (NED), Central Eastern Desert (CED), and Southern Eastern Desert (SED) [25]. The concentration of granitic rocks in NED and SED is higher than that of CED, while CED reveals the presence of a greater concentration of rocks with strong oceanic connections, such as ophiolites and Banded Iron-Formation (BIF) [26].

The western part of the area is occupied by sedimentary rocks of upper Cretaceous age, intercalated with Quaternary deposits. Moreover, the eastern side of the area is covered by igneous rocks of Paleozoic age (Figure 2). The exposed rock units can be classified into three main groups from older to younger units. The first group is characterized by the Pan-African ophiolites and island-arc assemblage [18]. The second group is related to the Cordilleran-stage associations, which includes different types of granites, while the third group is related to the Quaternary sediments [18, 27]. The fracture lineaments including faults have many trend sets; NE–SW, NNW–SSE, ENE–WSW and NE-SW, while the NE–SW is the major one.

4. Descriptions of Radioactive Element Maps

The interpretation of the four radioelements maps; TC (Figure 3a), K (Figure 3b), eU (Figure 3c) and eTh (Figure 3d) were performed. According to the results of the radioelements maps, the study area can be divided into three levels. The first low radiometric level (blue color) is < 2.7 µR/h for total count, < 0.4% of potassium, < 1.4 ppm equivalent uranium and < 3.6 ppm equivalent thorium. This level is well accompanied with metavolcanics, gabbroic rocks.

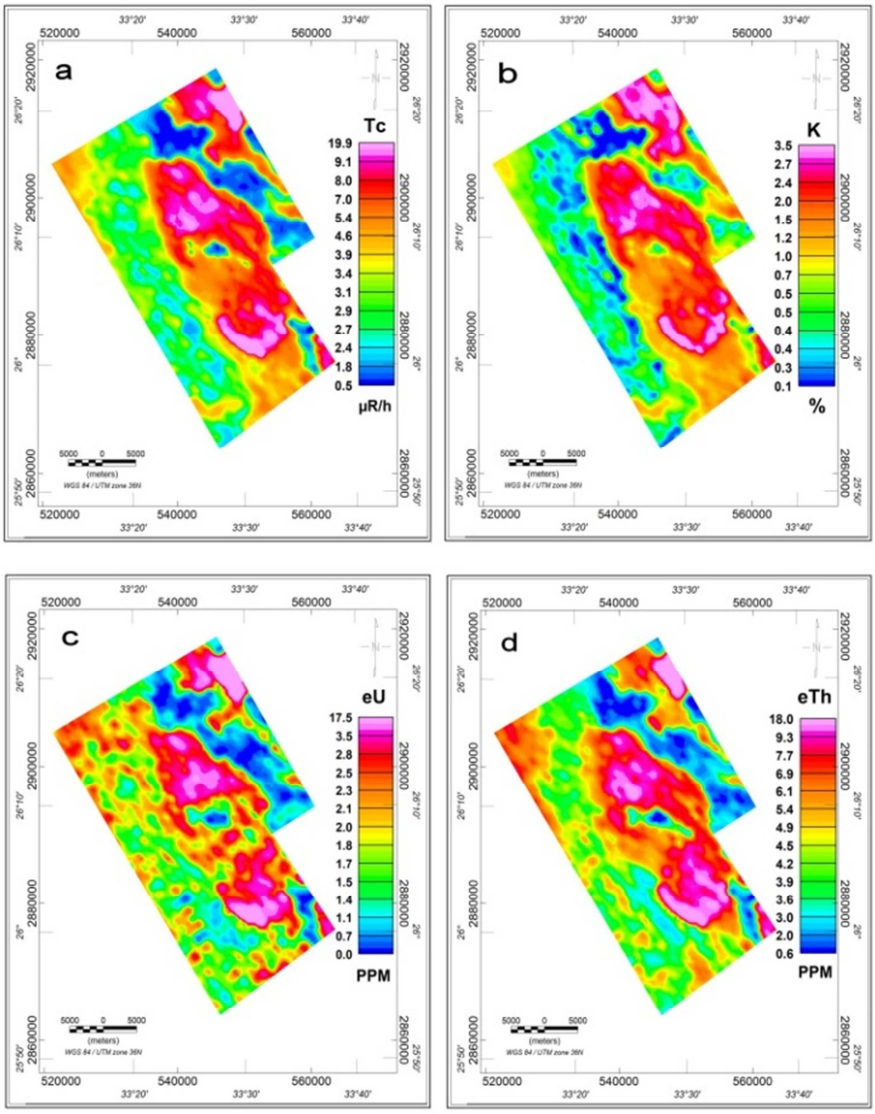

Figure 3. *a. Total Count Radiometric Data Map, b. Potassium Concentration Map, c. Equivalent Uranium Concentration Map, d. Equivalent Thorium Concentration Map of the study area.*

The second level (green color) ranges from 2.7 to 4.6 µR/h for total count, from 0.4 to 1.2% of potassium, from 1.4 to 2.1 ppm equivalent uranium and from 3.6 to 4.9 ppm equivalent thorium. This level is associated with Upper cretaceous Taref Formation, which is intercalated with quaternary deposits and some small spots of metavolcanics.

The third level (red color) ranges from 4.6 to more than 19.9 µR/h for total count, from 1.2 to 3.5% of potassium, from 4.9 to 17.5 ppm equivalent uranium and from 4.9 to 18 ppm equivalent thorium. This level is accompanied with the exposed igneous rocks such as Younger Granite, Post-Hammamat felsite, Dokhan Volcanics and Older Granite.

5. Detection of Hydrothermal Alteration Zones

The regions of K enrichment that are produced from the radiometric data can be used to illustrate the hydrothermal alteration zones such as potassic and phyllic altered zones. Thorium is known to be less mobile geochemically than potassium and uranium. Therefore, thorium (eTh) is used as a lithological background monitor to determine ideal eU and K values [29, 30].

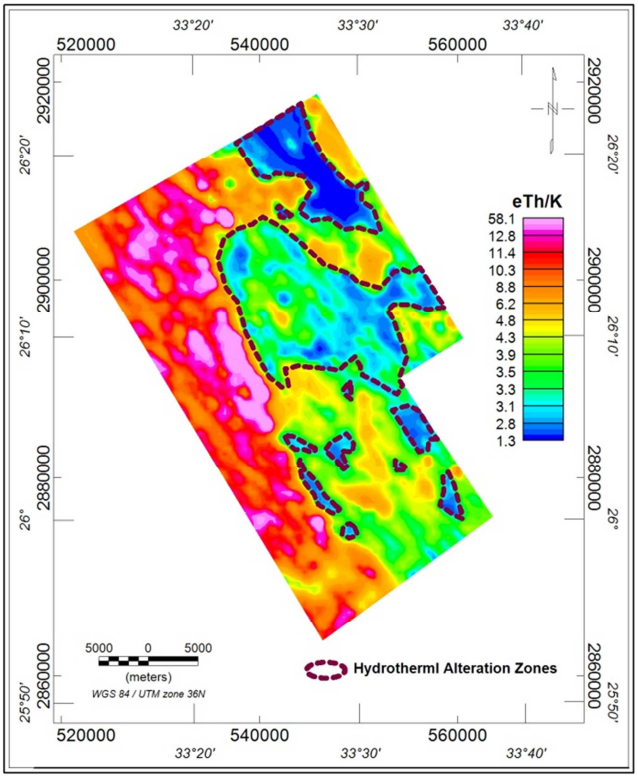

Figure 4. *Two-Radioelements (eTh/K) Ratio Map of the study area.*

Therefore, normalization of the radioactive data by eTh values is necessary to overcome the influences of environment, lithology, leaching and weathering on K and eU concentrations. To separate K enrichment which are relevant to hydrothermal alteration zones from those associated with lithology such as leaching and biochemical weathering effects, ratio of eTh concentration to the K counts (eTh/K map) (Figure 4) was generated. The Potassium Ternary Composite Image (Figure 5) of the study area is generated and compared with the (eTh/K map) (Figure 4) and hydrothermal alteration zones such as potassic and phyllic altered areas were detected.

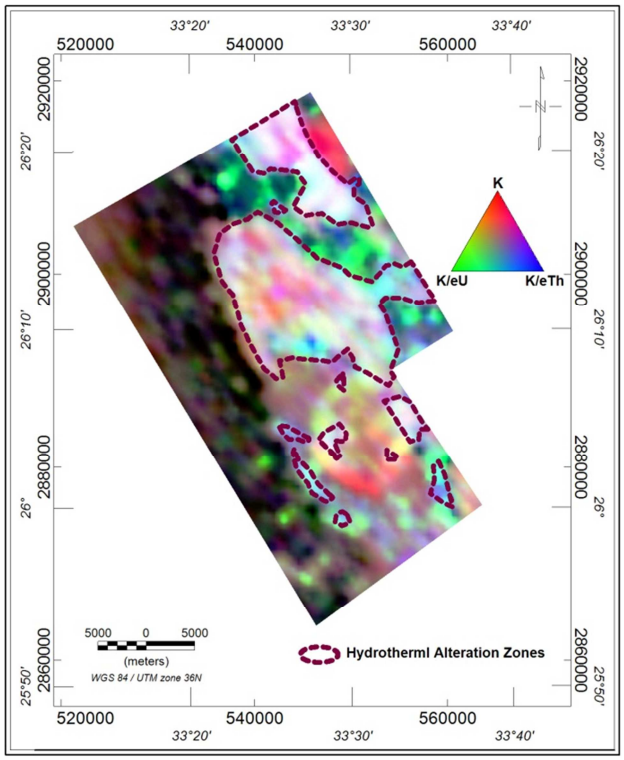

Figure 5. *Potassium Ternary Composite Image of the study area showing the potassic and phyllic altered zones.*

As thorium impoverishment often occurs with K enrichment during hydrothermal alteration processes [30]. The F-Parameter technique proposed by Efmov, 1978 [31] was also applied because it involves two significant relationships, the K richness correlated to eTh/eU ratio and eU richness correlated to the eTh/K ratio (equation. 1) [31]. F-Parameter is the ratio of the product of the K counts and the eU concentration to the eTh concentration. F-Parameter values were calculated as shown in Figure 6. The deviation from the ideal K values (Kd) proposed by Saunders et al., 1987 [32], is utilized in mapping hydrothermal alteration haloes. The nominal Kn values were computed from equation (2), where the values for K map average and eTh map average are obtained from the statistics of the K and eTh grids as 1.2% and 5.3 ppm, respectively. Deviation from the nominal K values (Kd) was considered to represent K enrichment values due to hydrothermal alteration processes as obtained by equation (1) and the map was generated as shown in Figure 7.

$$F = (k * eU)/eTh = eU/(eTh/K) \quad (1)$$

$$Kn = (K\ map\ average)/(Th\ map\ average) * Th\ map \quad (2)$$

$$Kd = (K - Kn)/Kn \quad (3)$$

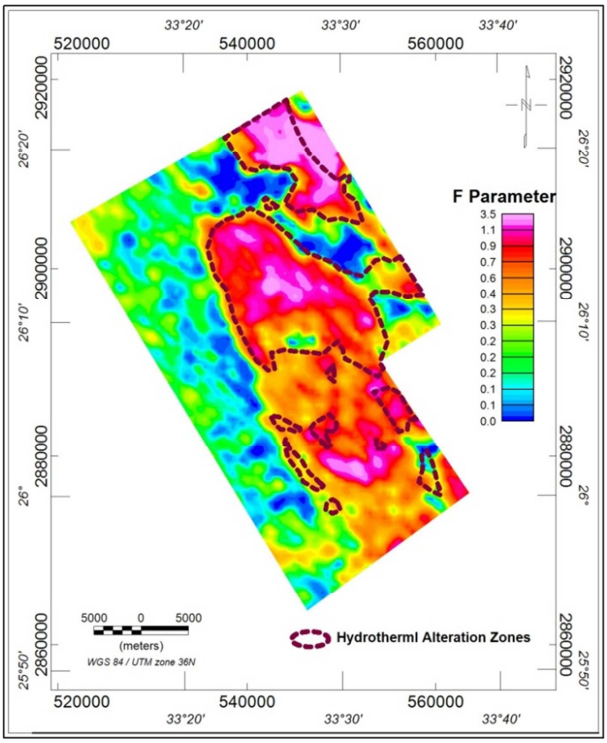

Figure 6. *F-Parameter Map of Efmov [31] of the study area.*

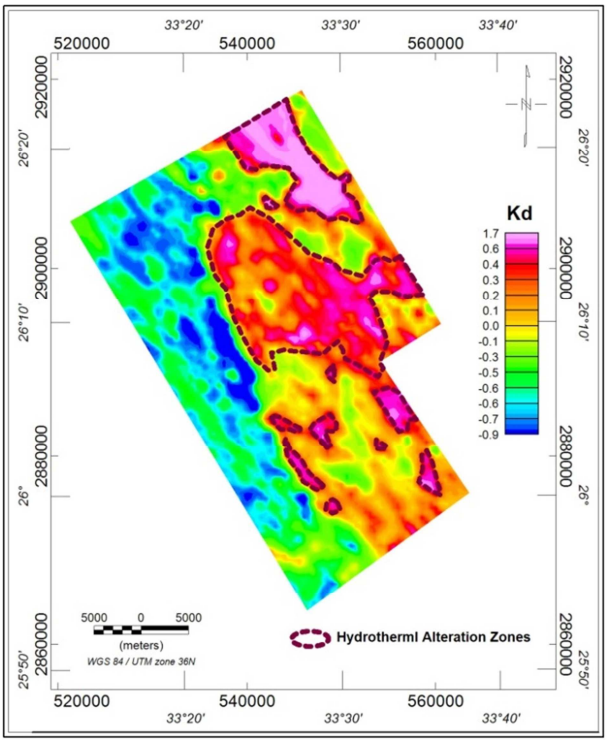

Figure 7. *Kd Map of Saunders et al. [32] (potassium anomalies) of the study area.*

The eTh/K ratio map (Figure 4), Potassium Ternary Composite Image (Figure 5), F-Parameter map (Figure 6) and Kd (potassium anomalies) (Figure 7) were analysed concurrently to detect the hydrothermal alteration haloes which are closely associated with orogenic gold mineralization. By examining the results of anomalously high Kd (0.3–1.7) and F-Parameter (0.6–3.5), as well as abnormally low eTh/K (1.3–3) and bright spots appearing on the Potassium Ternary Composite Image (Figure 5), the presence of highly fractured and hydrothermally altered zones within the study area was inferred. These signatures characteristically highlight potassium enrichment halos that are associated with the orogenic gold mineralization in the study area.

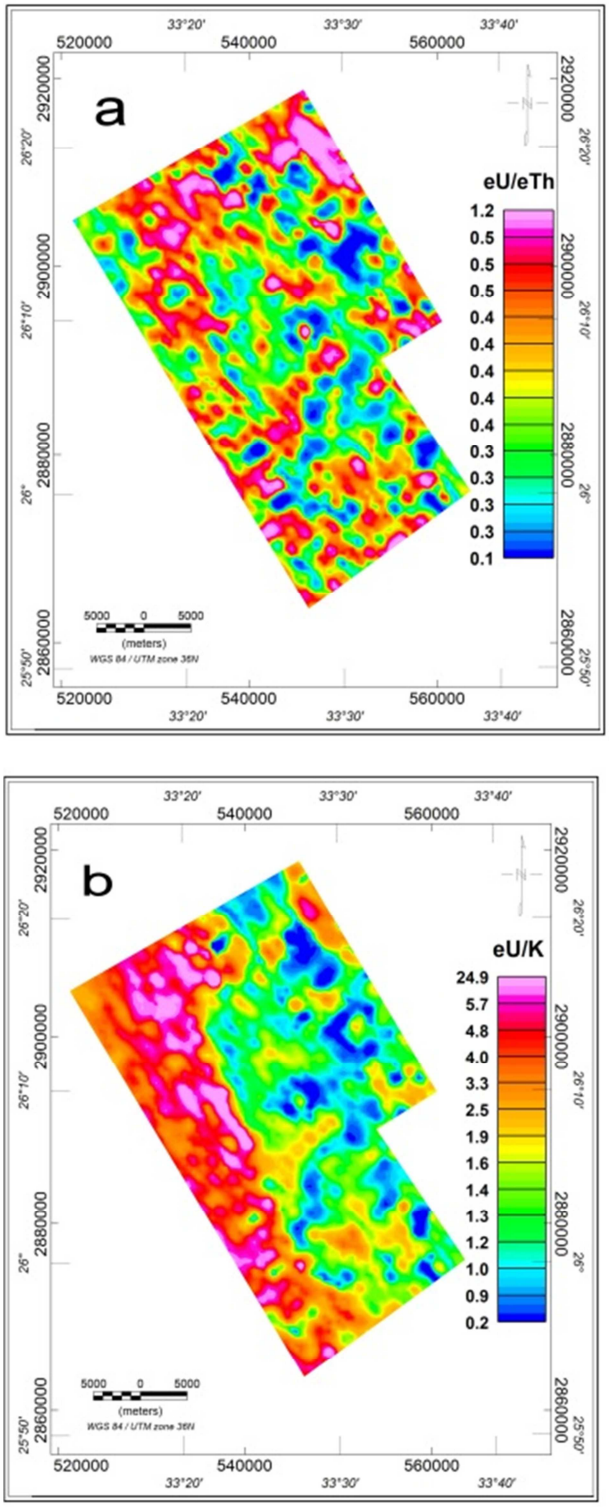

Figure 8. *Two-Radioelements Ratio Maps; a. (eU/eTh) Ratio Map, b. (eU/K) Ratio Map of the study area.*

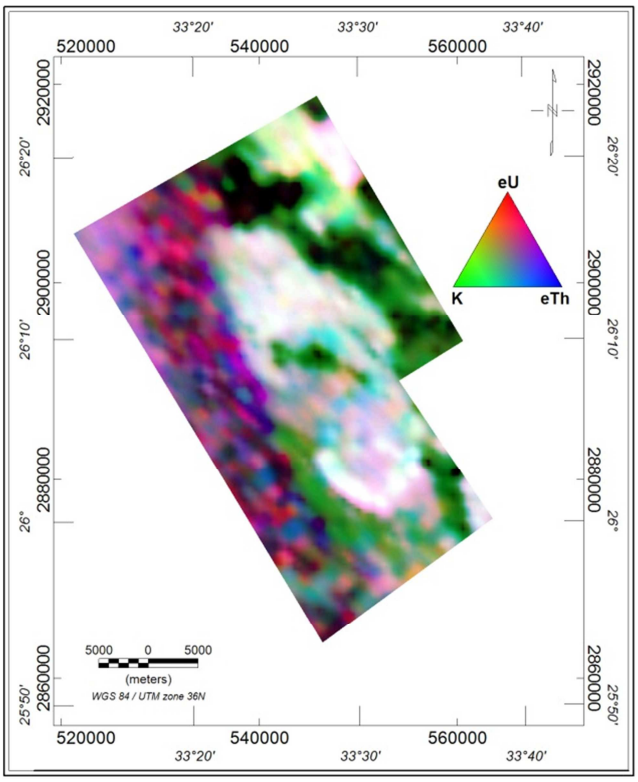

Figure 9. *Three radioelement ternary composite image of the study area.*

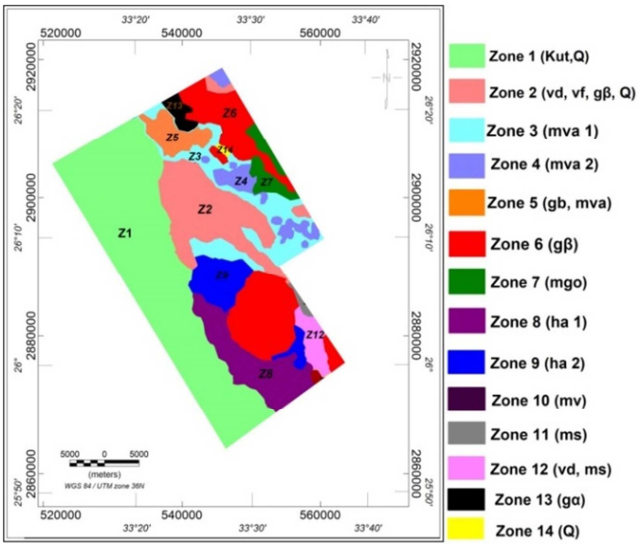

Figure 10. *Interpreted Radio-Spectrometric Zonation (IRSZ) Map of the study area.*

6. Ratio Radioelement Maps

Ratio maps of eU/eTh and eU/K are generated (Figures 8a and 8b). The values of the ratios eU/eTh and eU/K are variably distributed and scattered over different geological units. Higher ratio values of eU/eTh (more than 1.2) and eU/K (up to 24.9) corresponding to the Taref and Quseir Formations, and some parts of Younger Granite were detected. The increase in the ratio values of eU/eTh and eU/K on sedimentary rocks may be caused by the leaching process of uranium since it is mobile and leached. On the other hand, the lowest ratio values of eU/eTh (less than 0.1) and eU/K (less than 0.2) are associated with Dokhan Formation, metavolcanics, metasediments, and parts of younger and older granites.

7. Interpreted Radio-Spectrometric Zonation (IRSZ) Map

Gamma ray spectrometry data might be used to determine the rock units of the same litholigies, in addition to identifying the contacts of the constrained lithologies [33]. The three radioelement ternary composite image (Figure 9) is generated to show the variation that occurs in the three radioelements K, eU and eTh concentrations, which mainly reflects lithologic variations. The IRSZ map (Figure 10) is performed to show the correlation between the three radioelement ternary composite image (Figure 9) and the geological map (Figure 2). The majority of the rock units in the geologic map are matching with the radioelement composite image map, while in some locations; it has been difficult to discriminate between some rocks units as shown in Figure (10).

The IRSZ map is classified into 14 zones as follows:

Zone 1 is related to Taref Formation (kut), which consists of Fluviatile and locally eolian sandstone intercalated with quaternary deposits (Q) and colored in pale green in the IRSZ map (Figure 10). This zone occupies the western side of the study area. Such zone is characterized by a relatively medium radiometric response.

Zone 2 is located in the central part of the study area and characterized by a very high radiometric response. This zone includes three types of rock units that haven't been discriminated in the ternary composite image (Figure 9); however, the three rock units give a high radiometric response. This zone is colored pink in the IRSZ map (Figure 10). These three rock units of Paleozoic Era are:

Dokhan Volcanic (Vd): Calc alkaline andesitic to rhyolitic rocks.

Younger Granite (g_{β}): Calk- alkaline-weekly deformed granitic rocks.

Post- Hammamat felsite (vf): Felsite porphyry and Quartz porphyry.

Zone 3 consists of intermediate-acid metavolcanics and metapyroclastics. Such zone is characterized by an intermediate radiometric response and denoted by (mva 1). This zone is colored in cyan in the IRSZ map (Figure 10) and located in the northeastern part of the study area.

Zone 4 consists of intermediate to acid metavolcanics and metapyroclastics. Such zone is characterized by a very low radiometric response and denoted by (mva 2) and colored in light blue in the IRSZ map (Figure 10).

Zone 5 consists of intermediate to acid metavolcanics and metapyroclastics (mva), intercalated with some gabbroic rocks (gb). This zone is located in the northern part of the study area with low radiometric response and colored in orange in the IRSZ map (Figure 10).

Zone 6 is located at the northeastern, central and southeastern part of the study area and colored in red in the IRSZ map

(Figure 10). This zone is related to calk-alkaline-weekly deformed granitic rocks of Paleozoic Era, denoted by (g_β), and characterized by a very high radiometric response.

Zone 7 is related to ophiolitic metagabbro and located in the northeastern part of the study area. This zone is colored in green in the IRSZ map (Figure 10). Such zone is characterized by a relatively low radiometric response.

Zone 8 is related to molasses-type conglomerate to siltstone silicate (Hammamat clastics), denoted by (ha1) and colored in violet in the IRSZ map (Figure 10). It occupies the southwestern part of the study area. Such zone is characterized by a relatively moderate radiometric response.

Zone 9 is related to molasses-type conglomerate to siltstone silicate (Hammamat clastics), denoted by (ha 2) and colored in blue in the IRSZ map (Figure 10). It is located in the central and southern parts of the study area and characterized by a relatively high radiometric response.

Zone 10 consists of metavolcanics (mv). Such zone is characterized by moderate radiometric response. This zone is colored by maroon color in the IRSZ map (Figure 10). This zone is located in the southern part of the study area.

Zone 11 is related to metasediments and metamorphed shelf sediment sand volcanogenic rocks. This zone is denoted "ms" and colored in grey in the IRSZ map (Figure 10). This zone is located at the southeastern part the study area.

Zone 12 is associated with metasediments and metamorphed shelf sediment sand volcanogenic rocks (ms) as well as Dokhan Volcanic (Vd). This zone is colored in coral in the IRSZ map (Figure 10) and located at the southeastern part the study area. This zone is characterized by a low radioactive response.

Zone 13 is related to calk-alkaline, usually foliated quartzdioritic to granodioritic rocks (older granite) ($g\alpha$). This zone is characterized by high radiometric response and colored in black in the IRSZ map (Figure 10).

Zone 14 is related to Quaternary deposits of the Quaternary age and colored in yellow in the IRSZ map (Figure 10). It has a moderate radiometric response.

8. Location of Uranium Leads

The relative concentration of uranium with respect to both potassium and thorium are important diagnostic factors in the recognition of possible uranium deposits [34].

The main objective of aerial gamma-ray spectroscopic survey data is the delineation of expected boundaries of potential areas of uranium, where various rock units are enriched with uranium [35]. The most important parameters, which can be measured, are relative concentrations of uranium to thorium and uranium to potassium, in conjunction with uranium measurements. Therefore, the eU composite image (Figure 11) provides useful information regarding the identification of anomalous zones of enriched uranium concentration. This can be expressed by the following expressions:

$$eU > X+2S$$

$$eU/eTh \geq X+2S, \text{ and}$$

$$eU/K \geq X+2S$$

Where: "X" is the arithmetic mean and "S" is the standard deviation.

The map of uranium anomalies (Figure 12) shows six important sites, as these sites were calculated statistically and appeared to have a statistically high abundance in eU values, eU/eTh and eU/K ratio values.

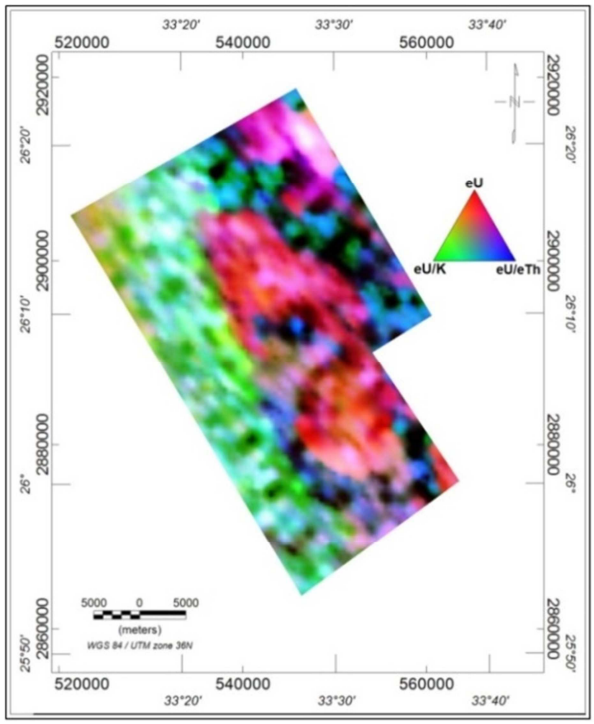

Figure 11. *Equivalent uranium ternary composite image of the study area.*

Figure 12. *The uranium anomaly map of the study area showing the six eU promising locations.*

These locations of uranium anomalies are of exploration importance and promising priority targets for ground geophysical and geological follow-up. These results are summarized in (Table 1).

Table 1. *Statistical values for Equivalent Uranium and its ratios.*

Rock Unit	Eleme-nt	Min	Max	Mean	Standard deviation	X+2S
	eU	0.205	3.80	1.78	0.41	2.6
Taref Formation (Kut)	eU/K	0.52	49.9	4.71	1.97	8.65
	eU/eTh	0.045	0.80	0.42	0.10	0.62
	eU	0.934	4.90	2.68	0.72	4.12
Post- Hammamat felsite (vf)	eU/K	0.49	2.12	1.11	0.25	1.61
	eU/eTh	0.16	0.6	0.36	0.07	0.5
	eU	0.36	18.831	3.53	2.56	8.65
Younger Granite (g_β)	eU/K	0.15	6.64	1.45	0.84	3.13
	eU/eTh	0.07	1.19	0.40	0.14	0.68
	eU	1.069	5.68	2.78	1.02	4.82
Quaternary deposits (Q)	eU/K	0.57	9.81	1.84	1.28	4.4
	eU/eTh	0.18	0.76	0.38	0.09	0.56

9. Conclusion

Gamma ray spectrometry method is widely used in various fields; it can be used for uranium exploration, geological mapping, and mineral exploration as well as for soil mapping. Airborne gamma ray spectrometry data were collected and interpreted over the Gabal Atalla and its surrounding area, Central Eastern Desert of Egypt. This study was conducted in order to determine the distribution of radioactive minerals (K40, U, Th), as well as to detect the potential uranium anomalies that can be studied in detail to verify them through ground studies.

Airborne spectrometric data processing was performed to generate different radiometric maps showing the radioactivity of the study area. The eTh/K ratio map (Figure 4), Potassium Ternary Composite Image (Figure 5), F-Parameter map (Figure 6) and Kd (potassium anomalies) (Figure 7) were analysed to detect the hydrothermal alteration zones which are closely associated with orogenic gold mineralization. It was observed that the abnormally high Kd (0.3-1.7) and F-Parameter (0.6-3.5), in addition to the abnormally low eTh/K (1.3-3), and bright spots appeared on the Potassium Ternary Composite Image (Figure 5) indicating to the highly fractured and hydrothermal regions within the study area. These signatures characteristically highlight K enrichment halos associated with the orogenic gold mineralization in the study area.

The statistical results showed that the generated map of uranium anomalies (Figure 12) includes six significant locations. These promising locations were calculated statistically and appear to have a statistically high abundance of eU, eU/eTh and eU/K values. These uranium anomalies are of exploration interest and promising priority targets for ground investigations. These results are summarized as high radiation associated with Taref Formation (Kut), Post-Hammamat felsite (vf), Younger Granite (g_β) and Quaternary deposits (Q). It was determined that these sites lie between three systems of structural lineaments by comparing these anomalies with the geological map of the study area.

Acknowledgements

The author would like to thank the Nuclear Materials Authority's Airborne Geophysics Department for allowing the data and software needed to accomplish this work.

References

[1] Graham, D., & Bonham-carter, G. (1993). Airborne radiometric data: a tool for reconnaissance geological mapping using a GIS. Photogramm Eng Remote Sensing 58 1243–1249.

[2] Andrson, H., & Nash, C. (1997). Integrated lithostructural mapping of the Rossing area, Namibia using high resolution aeromagnetic, radiometric, Landsat data and aerial photographs Exploration, Geophysics 28 185–191. https://doi.org/10.1071/EG997185

[3] Charbonneau, B W., Holman, P B., & Hetu R J. (1997) Airborne gamma spectrometer magnetic-VLF survey of northeastern Alberta. In Exploring for minerals in Alberta: Geological Survey of Canada Geoscience contributions, edited by MacQueen, Canada-Alberta agreement on mineral development Geological Survey of Canada Bulletin 500 107–132. https://doi.org/10.4095/209209.

[4] Jaques, A., Wellman, P., Whitaker, A., & Wyborn, D. (1997). High resolution geophysics in modern geological mapping, AGSO Journal of Australian Geology & Geophysics 17 159–174.

[5] Elawadi, I., Ammar, A., & Elsirafy, A. (2004). Mapping surface geology using airborne gamma-ray spectrometric survey data-A case study In proceeding in the 7th SEGI international Symposium-imaging Technology, Sendai-Japan 349–354.

[6] Lo, B., & Pitcher, D. (1996). A case history on the use of regional aeromagnetic and radiometric data sets for lode gold exploration in Ghana. Annual Meeting Expanded Abstracts Society of Exploration Geophysicists 592–595. https://doi.org/10.1190/1.1826712

[7] Grasty, R., & Shives, R. (1997). Applications of gamma ray spectrometry to mineral exploration and geological mapping, Workshop presented at Exploration 97: Fourth Decennial Conference on Mineral Exploration.

[8] Cook, S., Corner R., Groves P., & Grealish, G. (1996). Use of airborne gamma radiometric data for soil mapping, Aust. J. Soil Res 34 183–194. https://doi.org/10.4095/20920910.1071/SR9960183.

[9] Wilford, J., Bierwirth, P., & Craig, M. (1997). Application of airborne gamma-ray spectrometry in soil/regolith mapping and applied geomorphology AGSO Journal of Australian Geology and Geophysics 17 201–216.

[10] Sanderson, D., Allyson, J., Tyler, A., & Scott, E. (1995). Environmental applications of airborne gamma ray spectrometry Application of Uranium Exploration Data and Techniques in Environmental Studies, IAEA-TECDOC-827, IAEA, Vienna, 71–79.

[11] Ford, K., Savard, M., Dessau, C., & Pellerin, E. (2001). The role of gamma-ray spectrometry in radon risk evaluation: A case history from Oka, Quebec. Geoscience Canada, 28, 2.

[12] Lahti, M., Jonsen, D., Multala, J., & Rainey, M. (2001). Environmental applications of airborne radiometric surveys. Expanded Abstracts, 63rd Annual Conference, European Association of Geoscientists and Engineers.

[13] Ismail, A. (1999). Evaluation of digitally -processed aerial gamma-ray spectrometric and magnetic data for geologic mapping, mineral exploration and monitoring of environmental radioactivity, abu-had area, central eastern desert, Egypt, Ph.D. Ain Shams university.

[14] Atef, A M., El-Arabi, H Sh., & Tamer, M R. (2014). Uranium possibilities at El Gilf El Kiber area, Southwestern part of the Western Desert, Egypt, IOSR-JAGG 2 (6) 36–43. https://iosrjournals.org/iosr-jagg/papers/vol2-issue6/Version-1/G02613643.pdf.

[15] Darnley, A., & Ford, K. (1989). Regional airborne gamma-ray syrvey: A review; in "Proceedings of Exploration 87: Third Decennial International Conference on Geophysical and Geochemical Exploration for Minerals and Ground Water" Geol. Surv. of Canada, Special 3 960 p.

[16] Wilford, J. (2002). Airborne gamma-ray spectrometry, Geophysical and Remote Sensing Methods for Regolith Exploration, Open File Report 144 p. 46–52.

[17] Aero Service., (1984). Final operational report of airborne magnetic/radiation survey in the Eastern Desert, Egypt, Aero Service Division, Houston, Texas, April, Six Volumes.

[18] Elkhadragy, A A., Abdelaziz, A M., Abdelmohsen G N., & El-Husseiny, A. (2016). Geological Mapping and Uranium Exploration at Qena-Quseir Shear Zone Area, Eastern Desert, Egypt, GJSFR 16 (5) 29–48. https://journalofscience.org/index.php/GJSFR/article/view/1935.

[19] Farahat, E., El-Mahalawi M., & Hoinkes, G. (2004). Continental back-arc basin origin of some ophiolites from the Eastern Desert of Egypt. Mineralogy and Petrology 82 81–104. https://doi.org/10.1007/s00710-004-0052-6.

[20] Saleh, A., (2020). Paleomagnetism of Late Neoproterozoic African Dike Swarms from the South Eastern Desert and the Paleo-Neoproterozoic Dataset from EgyptPure and Applied Geophysics 177 (11) 1–12. https://doi.org/10.1007/s00024-020-02562-5.

[21] Stern, B., Gottfried, D., & Hedge, C. (1984). Late Precambrian rifting and crustal evolution in the NE desert of Egypt, Geology 12 (3). https://doi.org/10.1130/0091-7613(1984)12<168:LPRACE>2.0.CO;2.

[22] Nairn, A., Ressetar, R., & Davies, J. (1980). Paleomagnetic results from Pan-African rocks of the Egyptian Eastern Desert, Annals Geol., Surv Egypt, 10 1013–1026.

[23] Meneisy, M. (1990). Volcanicity-In Said, R (ed), The Geology of Egypt, Rotterdam, Balkema; p. 157–172.

[24] Liégeois, J., & Stern, R. (2010). Sr–Nd isotopes and geochemistry of granite–gneiss complexes from the Meatiq and Hafafit domes, Eastern Desert, Egypt: no evidence for pre-Neoproterozoic crust. Int. J. Earth Sci, 57, 31–40. https://doi.org/10.1016/j.jafrearsci.2009.07.006.

[25] El-Ramly, M. (1972). A new geological map for the basement rocks in the Eastern and south Western Deserts of Egypt, (1:1,000,000). Ann. Geol. Surv. Egypt, 11 1–18.

[26] Sultan, M., Arvidson, R., Duncan, I., Stern, R., & EL-Kaliouby, B. (1988). Extension of the Najd Shear System from Saudi Arabia to the Central Eastern Desert of Egypt based on integrated field and Landsat observations, Tectonics, 7, 1291-1306. https://doi.org/10.1029/TC007i006p01291.

[27] El-Gaby, S., (1983). Architecture of the Egyptian basement complex Proceedings of the Fifth Intern. Conf. on Basement Tectonics, Cairo, Egypt.

[28] Conoco Inc., (1987). Stratigraphic lexicon and explanatory notes to the geological map of Egypt 1:500,000. Conoco Inc, Cairo, Egypt, p. 262.

[29] Watanabe, Y., Sato R., & Sulaksono, A. (2018). Role of Potassic Alteration for Porphyry Cu Mineralization: Implication for the Absence of Porphyry Cu Deposits in Japan. https://doi.org/10.1111/rge.12165.

[30] Sanusi, S O., & Amigun, J O. (2020). Structural and hydrothermal alteration mapping related to orogenic gold mineralization in part of Kushaka schist belt, North-central Nigeria, using airborne magnetic and gamma-ray spectrometry data, SN Appl. Sci, 2 1591. https://doi.org/10.1007/s42452-020-03435-1

[31] Efmov, A. (1978). Multiplicative indicator for the identification of endogenous ores by airborne gamma spectrometric data in Methods of Ore Geophysics. Leningrad, Scientific and Production association Geofzica, Ed: 59-68.

[32] Saunders, D., Terry, S., & Thompson, C. (1987). Test of national uranium resource evaluation gamma-ray spectral data in petroleum reconnaissance. Geophysics, 52 (11) 1547–1556.

[33] Duval, J. (1983). Composite colour images of aerial gamma -ray spectrometric data. Geophysics, 48 (16) 722–735. https://doi.org/10.1190/1.1441502.

[34] El Arafy, R., Nady, A., Al-Ibiary, M., Nabeh, M., & Abdeen, S. (2019). Use of Remote Sensing and Gamma Ray Spectrometric Data for Elucidating Radioactive Mineralized Zones, Wadi Jararah-Wadi Kharit Area, South Eastern Desert, Egypt, GJSFR 19 (1) 55–73.

[35] Saunders, D., & Potts, M. (1976). Interpretation and application of high sensitivity airborne gamma ray spectrometric data. In: IAEA Symp. Exploration for Uranium Ore Deposits, Vienna, pp. 107–124.